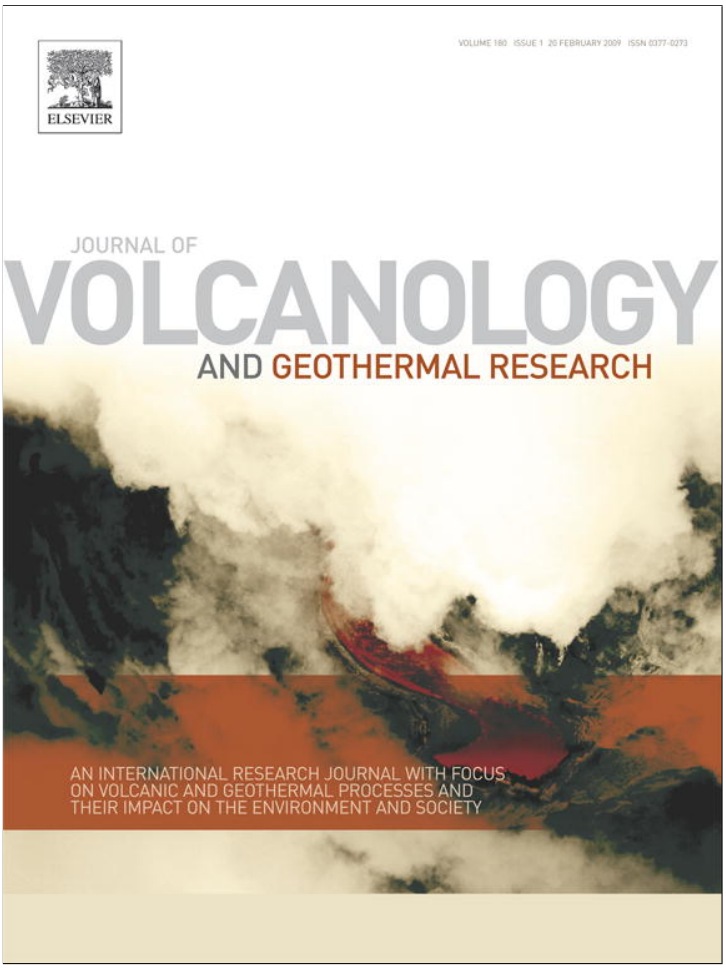

Journal of Volcanology and Geothermal Research 180 (2009) 67–80

Contents lists available at ScienceDirect

Journal of Volcanology and Geothermal Research

journal homepage: www.elsevier.com/locate/jvolgeores

The P-wave velocity structure of Deception Island, Antarctica, from two-dimensional seismic tomography

Tami Ben-Zvi [a], William S.D. Wilcock [b,*], Andrew H. Barclay [c], Daria Zandomeneghi [d], Jesús M. Ibáñez [d], Javier Almendros [d]

[a] Department of Earth and Space Sciences, University of Washington, Box 351310, Seattle, WA 98195-1310, USA
[b] School of Oceanography, University of Washington, Box 357940, Seattle, WA 98195-7940, USA
[c] Lamont-Doherty Earth Observatory, Palisades, NY 10964, USA
[d] Instituto Andaluz de Geofísica, University of Granada, Campus de Cartuja, s/n, Granada, 18071, Spain

ARTICLE INFO

Article history:
Received 19 June 2008
Accepted 13 November 2008
Available online 28 November 2008

Keywords:
tomography
magma chamber
Deception Island

ABSTRACT

Deception Island is a volcanic island with a flooded caldera that has a complex geological setting in Bransfield Strait, Antarctica. We use P-wave arrivals recorded on land and seafloor seismometers from airgun shots within the caldera and around the island to invert for the P-wave velocity structure along two orthogonal profiles. The results show that there is a sharp increase in velocity to the north of the caldera which coincides with a regional normal fault that defines the northwestern boundary of the Bransfield Strait backarc basin. There is a low-velocity region beneath the caldera extending from the seafloor to >4 km depth with a maximum negative anomaly of 1 km/s. Refracted arrivals are consistent with a 1.2-km-thick layer of low-velocity sediments and pyroclastites infilling the caldera. Synthetic inversions show that this layer accounts for only a small portion of the velocity anomaly, implying that there is a significant region of low velocities at greater depths. Further synthetic inversions and melt fraction calculations are consistent with, but do not require, the presence of an extensive magma chamber beneath the caldera that extends downwards from ≤2 km depth.

1. Introduction

A common model for volcanoes envisions that they are underlain by one or more fully or partially molten crustal magma chambers that store magma supplied from depth (e.g., Marsh, 1989). The magma chambers may be fully molten sills or blob-like features, zones of partially molten mush, or networks of magma filled cracks. Knowledge of the location, size and structure of magma chambers provides a critical constraint for relating observations of the morphology, petrology, and eruption history of volcanoes to their internal mechanics. Since elevated temperatures and the presence of melt significantly reduce seismic velocities, seismic imaging techniques are frequently applied in volcanic environments (e.g., Iyer, 1992; Iyer and Dawson, 1993; Lees, 2007).

In continental settings, a variety of seismic techniques have been used to detect subsurface magma. At a few locations mid-crustal magma sills have been imaged using reflected phases (e.g., Sanford et al., 1977; Mizoue et al., 1982). At several others upper crustal magma chambers have been inferred from the presence of seismic shadow zones (e.g., Matumoto, 1971; Einarsson, 1978; Horiuchi et al., 1997). The amplitude characteristics of body waves can also be inverted to image regions of high attenuation associated with magma accumulations (e.g., Sanders et al., 1988; Sanders, 1993). However, travel time tomography is by far the most common volcano imaging technique and has been applied to numerous continental volcanoes, most often using local or teleseismic earthquake sources (Iyer, 1992; Iyer and Dawson, 1993; Lees, 2007).

At some large volcanic systems, travel time tomography resolves large-magnitude low-velocity anomalies that are likely associated with substantial accumulations of partial melt. For example, at the Toba Caldera complex in Northern Sumatra, one of the largest active volcanic system in the world, local earthquakes have been used to invert for P-wave velocities in a coarse model with a grid measuring $10\times10\times\sim10$ km^3 (Masturyono et al., 2001). The results reveal crustal low-velocity anomalies of up to 37%. In the continental USA, teleseismic arrivals have been used to map low-velocity anomalies of 20–30% at ~10 km depth in the Long Valley (Weiland et al., 1995) and Valles calderas (Lutter et al., 1995), while similar anomalies have been imaged in Yellowstone with local earthquakes and explosive sources (Miller and Smith, 1999).

In contrast, at smaller continental volcanoes travel time tomographic studies usually either fail to detect low-velocity regions or only image low-velocity anomalies with small magnitudes (≤~10%) that require small degrees of partial melt at most (e.g., Iyer and Dawson, 1993; Lees, 2007). In some settings shallow magma accumulations may not exist but in others the failure of travel time tomography to detect them reflects the limited resolution of the method. Seismic tomography depends on illuminating the target with

* Corresponding author. Tel.: +1 206 543 6043; fax: +1 206 543 6073.
E-mail address: wilcock@u.washington.edu (W.S.D. Wilcock).

0377-0273/$ – see front matter © 2008 Elsevier B.V. All rights reserved.
doi:10.1016/j.jvolgeores.2008.11.020

a large number of seismic waves from many angles (Iyer, 1992; Lees, 2007). Good ray geometries can be difficult to achieve with local earthquake sources because they tend to be clustered. Teleseismic sources may yield better ray distributions, but their long wavelength limits resolution. There are practical difficulties associated with acquiring large active-source data sets. In this respect, studies in the marine environment have a big advantage because they can take advantage of airguns (and historically explosives) to generate a high density of sources.

In deep-water settings, seismic techniques have detected substantial accumulations of crustal melt beneath fast and intermediate spreading-rate mid-ocean ridges. Multichannel seismic reflection studies image the roofs of sill-like magma chambers at 1–3 km depth (e.g., Detrick et al., 1987) and can be used to infer the presence of fully or significantly molten thin melt lenses extending tens of kilometers along axis, ~1 km across and ~100 m in depth (e.g., Hussenoeder et al., 1996; Kent et al., 1990). In the same settings, P-wave tomographic images obtained by recording airgun and explosive sources with ocean bottom seismometers (OBSs) have resolved low-velocity regions extending below the axial magma lens, that have maximum velocity anomalies of 30–40% and are interpreted quantitatively in terms of substantial accumulations of partial melt (Dunn et al., 2000; West et al., 2001).

Partially submerged volcanoes in shallow marine environments provide a setting in which it is possible to combine a large number of land stations and ocean bottom seismometers with artificial sources in the surrounding waters. This configuration has been used effectively at the Rabaul Volcano, an arc volcano with a flooded 8 km×14 km caldera in Papua New Guinea (Finlayson et al., 2003). Explosive sources were combined with regional earthquake sources to image a low-velocity zone at 3–6 km depth with anomalies reaching 24% that was interpreted as a magma reservoir. At Campi Flegrei caldera, airgun shots have been combined with local earthquakes to obtain images of a low V_P and low V_P/V_S anomaly at 2–4 km depth which is interpreted in terms of over-pressured gas (Chiarabba and Moretti, 2006).

The geometry of partially submerged volcanoes is particularly attractive for tomography if airguns can be fired all around the island and also within a flooded caldera above the center of the volcano. Deception Island is one of a relatively small number of volcanic islands that allows this configuration; it is a small horseshoe shaped island with a flooded caldera that is accessible through a narrow opening to the open sea. In this paper, we present two-dimensional tomographic images along two orthogonal profiles across Deception Island that are obtained from data collected during a three-dimensional seismic tomography experiment. The seismic data are used to understand the structure of the volcano and to infer the possible presence of a substantial accumulation of shallow melt beneath the caldera.

2. Geological background

Deception Island is an active strato-volcano at the southwest end of Bransfield Strait, a backarc basin that developed as a result of asymmetric extension between the South Shetland Islands and the Antarctic Peninsula (Fig. 1). The South Shetland island arc formed as the result of the subduction of the Phoenix plate beneath the Antarctic plate. The rate of subduction decreased dramatically at about ~4 Ma (Barker, 1982) and continues today, if at all, only very slowly

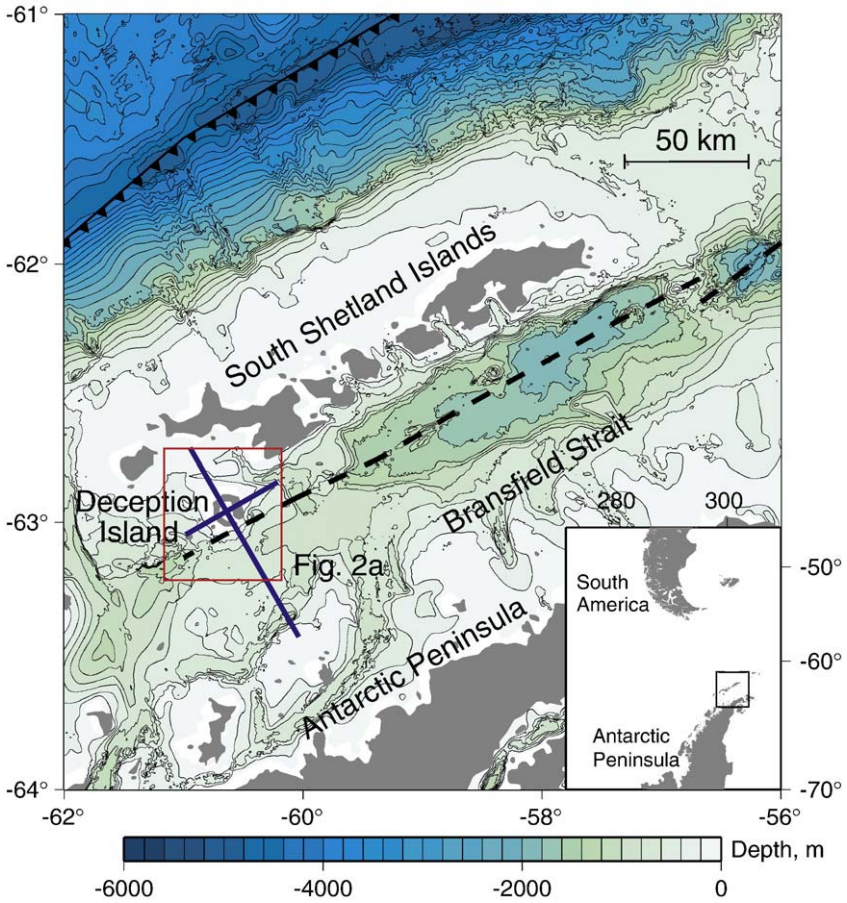

Fig. 1. Location of Deception Island in Bransfield Strait which separates the Antarctic Peninsula to the southeast and the South Shetland Islands to the northwest. The bold solid lines show the location of the seismic refraction profiles analyzed in this study and the faint box shows the area covered by Fig. 2a. The bathymetry data are from the Marine Geoscience Data System and the bathymetric contours clearly delineate asymmetric extension across the Bransfield Strait. Also displayed are the subduction zone north of South Shetland Islands (hatchured line) and the approximate locus of spreading in the Bransfield Strait (dashed line). The inset figure shows the location of Bransfield Strait relative to South America and the Antarctic Peninsula.

(Robertson et al., 2002). The decrease in convergence rates led to the onset of the current extensional regime in Bransfield Strait that propagated from the northeast to the southwest and is believed to be driven by some combination of slab rollback (Barker and Austin, 1998; e.g., Barker, 1982; Larter et al., 1991) and trans-tension resulting from left-lateral slip along the Shackleton Fracture Zone and South Scotia Ridge (e.g., Klepeis and Lawver, 1996; Maestro et al., 2007). There are differing opinions on crustal thickness beneath Bransfield Strait (Christeson et al., 2003; Janik et al., 2006) but it is clear that extension has not progressed to the formation of oceanic crust.

Deception Island forms the boundary between the Central and Western Bransfield Basins and its footprint extends from the northeastern boundary of the basin to the axis of backarc extension. The emerged top of the volcano is a small horseshoe shaped island with a diameter of ~15 km that encircles a flooded caldera, named Port Foster, measuring 5–9 km across with a narrow opening to the sea. The volcano has erupted several times historically (Smellie et al., 2002), most recently in a series of small eruptions in 1967–1970. Its age is poorly constrained; normal magnetic polarities require an age less than 800 Ka and limited field evidence and a single K–Ar date suggest an age <100–200 Ka (Keller et al., 1991a; Smellie, 2001). It has a mean composition of basaltic–andesite to basalt and enigmatic petrological characteristics that indicate both arc and backarc influences (Keller et al., 1991b, 2002).

Deception Island's caldera has traditionally been considered a classic volcanic collapse caldera (Baker et al., 1975), although extensive deposits from the caldera forming eruption have yet to be identified. Motivated by the lack of evidence for the formative eruption and also by the absence of known ring faults and radial dikes, Martí et al. (1996) interpreted fault patterns around the caldera in terms of an alternative model in which the caldera formed as a passive response to regional extension in two directions. More recently, Smellie (2001) interprets the lithostratigraphy to support a model in which mixing of two magma types led to an explosive eruption with collapse occurring on intersecting faults that had been formed by regional extension. He estimates the size of the caldera forming eruption to be ~30 km^3.

Bransfield Strait and environs have been the focus of many regional-scale seismic experiments that have sought to understand the structure of the backarc rift and the tectonics of the region (e.g., Grad et al., 1997; Barker and Austin, 1998; Robertson et al., 2002; Christeson et al., 2003). However, on Deception Island itself, seismic experiments have been limited to shallow seismic reflection (e.g., Rey et al., 2002) and refraction (Grad et al., 1992) imaging of sediment layers in the caldera and to the deployment of small networks and arrays for monitoring earthquakes and emergent signals (e.g., Ibáñez et al., 2003). To date the only constraints on deeper structure have come from potential field (Muñoz-Martín et al., 2005) and geothermal observations (Ortiz et al., 1992), both of which have been used to infer the presence of shallow magma.

3. Seismic experiment

The seismic data were collected using the *R/V Hesperides* in January 2005 as part of an international experiment led by the University of Granada, Spain. The experiment was designed to obtain a high-resolution three-dimensional image of a volume extending up to ~20 km from the center of the caldera and down to at least ~3 km depth, and also included a 90-km-long profile for deeper imaging of the crust beneath the island (Fig. 2a). For logistical reasons, two rounds of shooting were undertaken with different instrument locations but very similar shot configurations. Data were recorded on three-component seismometers at 36 land stations and by 9 compact arrays which typically comprised about ten vertical seismometers arranged around one of the three-component seismometer sites. Land stations were not deployed uniformly (Fig. 2b) due to glacier coverage and the difficult access to parts of the island. Fourteen 1-Hz ocean bottom seismometers (OBS) from the US OBS Instrument Pool were also available for each round of shooting and were deployed at a total of 26 seafloor sites within the caldera and around the island. Because of a software problem, data were only obtained from 14 seafloor sites.

For shooting we used an array of six airguns with a total volume of 57 l (3500 in^3). In the caldera, shots were fired at a spacing of 120 m on a 0.5 km grid. Outside the caldera shots were fired at a spacing of 170–340 m on three circumferential lines at distances of 10, 15, and 20 km from the center of the island and on eight radial lines each of which extended at least 25 km from the center of the island. Two of the radial

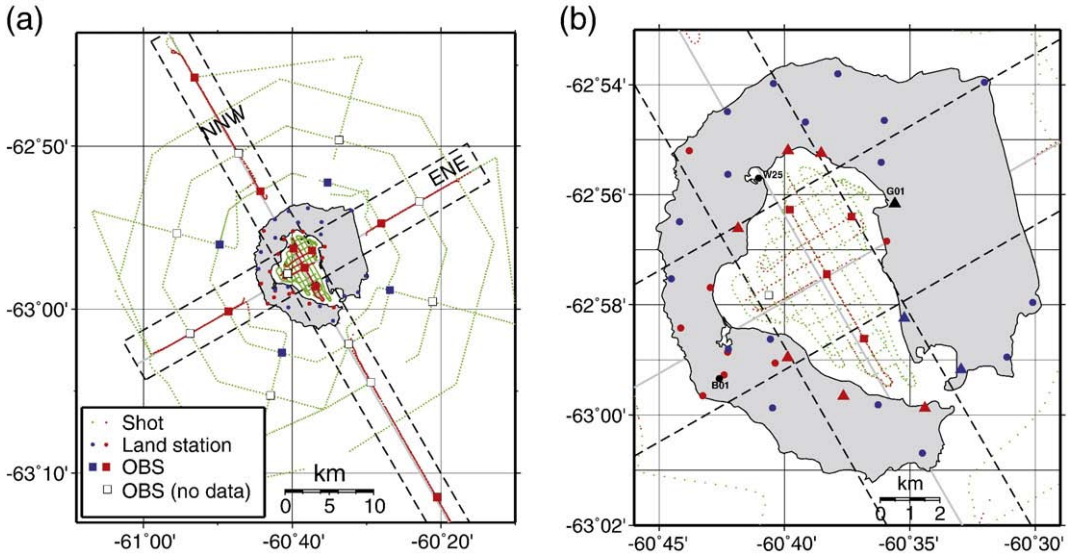

Fig. 2. (a) Experiment design showing the location of seismic stations and arrays on land stations (circles) and ocean bottom seismometers (OBSs) (squares) in both rounds of shooting, and airgun shots for the first round of shooting (dots). Shots for the second round had a similar configuration. Red symbols (black symbols in the black and white version) in corridors that are enclosed by dashed lines show the stations and shots used for two-dimensional inversions presented in this paper. (b) Same as (a) except showing a smaller area around the island. The seismic antennae in this figure are shown by triangles; a single vertical seismometer from each antenna array with a red symbol was included in this study. Stations for which data are shown in this paper are labeled with the station name.

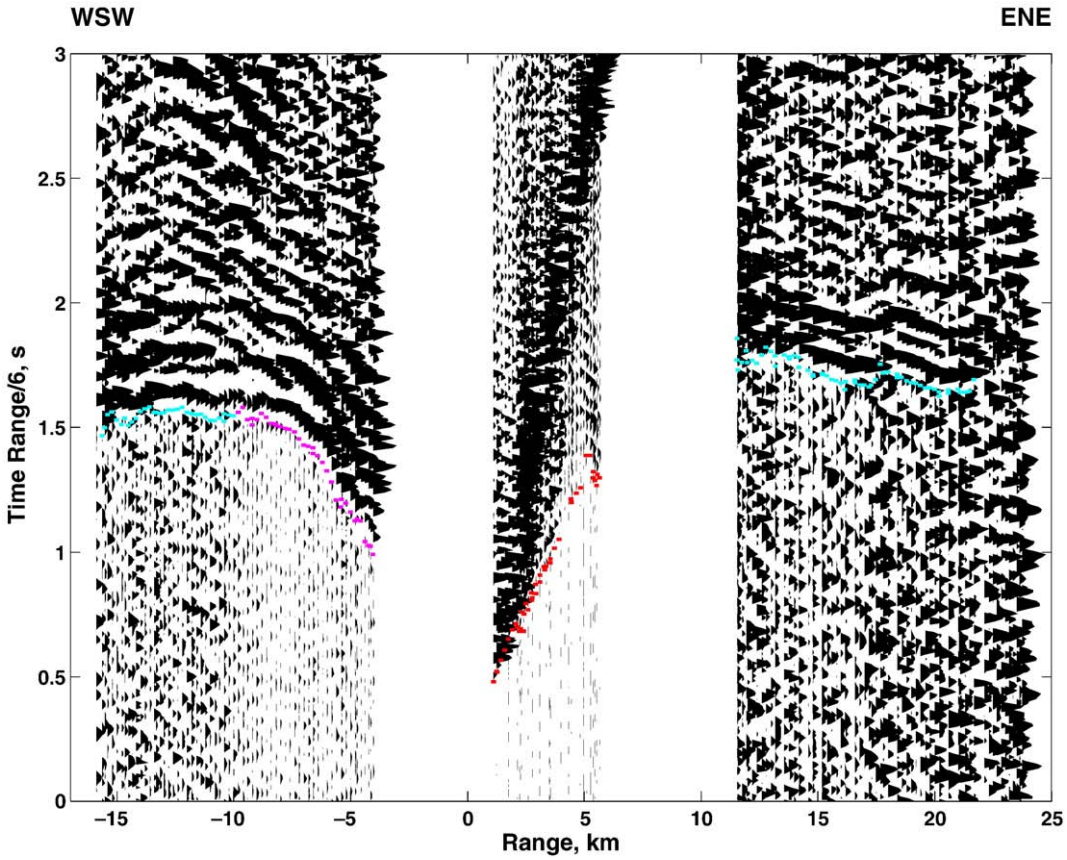

Fig. 3. Example of a record section for the WSW–ENE profile recorded by station B01 (labeled in Fig. 2b), located on land to the southwest of the caldera, plotted with a reduction velocity of 6 km/s. A water path correction has been applied to correct the shot ranges and times to the ray entry point on the seafloor. First arrival picks are shown with horizontal ticks that are color coded to indicate estimated uncertainties as follows: red = 10 ms; magenta = 20 ms; cyan = 40 ms (pick uncertainties are shown by annotations in the black and white version).

lines were extended to create the 90-km-long refraction profile. In this paper, we present the results of two-dimensional inversions along the 90 km refraction profile oriented NNW–SSE and along a 55-km-long profile oriented WSW–ENE (Figs. 1 and 2a). Three-dimensional inversions for shallow volcano structure are the subject of a separate study (Zandomeneghi et al., 2007, submitted for publication).

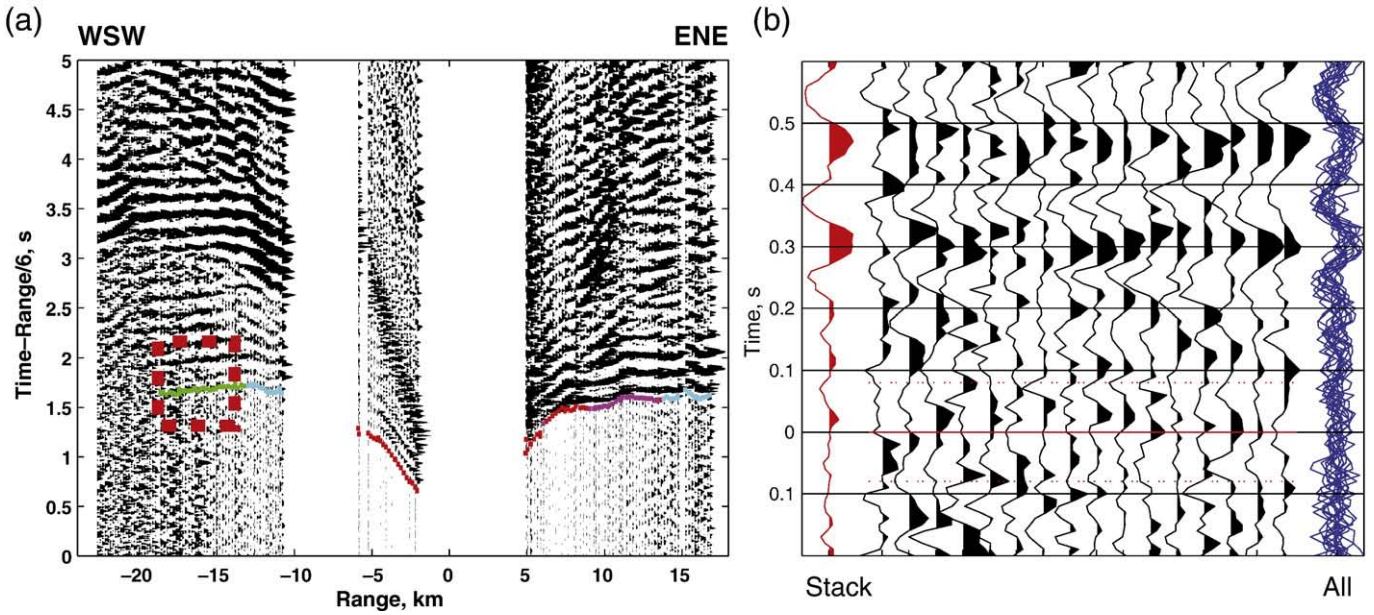

Fig. 4. (a) Example of a record section for the NNE–SSW profile recorded by station G01 (labeled in Fig. 2b), a land station located east of the caldera, plotted with a reduction velocity of 6 km/s. A water path correction has been applied to correct the shot ranges and times to the ray entry point on the seafloor. Pick uncertainties are shown as for Fig. 3 with green representing estimated uncertainties of 80 ms. For this station, the arrivals enclosed by a dashed box are visible but have a very low signal to noise. (b) To pick these arrivals we used cross-correlation to align arrivals, and made the pick from a stack (left trace) of the aligned waveforms (see text).

4. Travel time data

Fig. 3 shows an example of a typical record section for shots on the WSW–ENE profile recorded by station B01 (labeled in Fig. 2b) in the southwestern part of the island. With the exception of a few intervals when background noise levels increase substantially for unknown reasons, the signal to noise ratio is high at shorter ranges and first arrivals can be picked directly. At ranges exceeding ~30 km, the signal to noise ratio is often low and the first arrivals emergent. This is particularly so for paths that pass beneath the island. To pick first arrivals with low signal to noise ratios, we implemented a cross-correlation and stacking technique (Fig. 4). Groups of arrivals were first stacked based on preliminary relative picks and then a 0.6-s-long section of each arrival was cross-correlated with the stack to obtain adjustments to the relative picks. The arrivals were then stacked again based on the new relative picks and the process repeated until the alignment converged. An absolute pick was then made from the final stack and assigned to each arrival based on the relative picks. For all travel time data, we assigned nominal pick uncertainties of 0.01, 0.02, 0.04 or 0.08 s, depending on a qualitative assessment of the pick quality (Figs. 3 and 4). For the NNW–SSE profile the data set comprises 2793 arrival time picks from 627 shots and 16 stations located within a 4-km-wide corridor. For the WSW–ENS profile, there are 1325 arrivals for 280 shots and 11 stations located within a 5-km-wide corridor.

5. Inversion method

We inverted the travel times of first arrivals with the marine tomography algorithm of Toomey et al. (1994) which utilizes a shortest path ray tracer (Moser, 1991), incorporates accurate corrections for the water path based on bathymetry, and implements separate grids for the forward ray tracing problem and for the inversion with linear interpolation between grid points. Both grids are hung from the bathymetry and topography and all of our results are referenced to this surface. For this study, we traced rays through a three-dimensional grid with a spacing of 200 m. For the inverse problem a two-dimensional velocity perturbation grid was used with spacing of 500 m. The inversion minimizes a functional s^2 given by

$$s^2 = \mathbf{d}^T \mathbf{C}_d^{-1} \mathbf{d} + \lambda_p \mathbf{m}^T \mathbf{I} \mathbf{m} + \lambda_v \mathbf{m}^T \mathbf{S}_v \mathbf{m} + \lambda_h \mathbf{m}^T \mathbf{S}_h \mathbf{m}$$

where **d** is a vector of travel time delays; $\mathbf{C}_d$ is the data covariance matrix; **m** a vector of slowness perturbations; **I** is the identity matrix with dimensions corresponding to the number of model parameters; $\mathbf{S}_v$ and $\mathbf{S}_h$ are second-order difference operators acting in the vertical and horizontal directions, respectively; λ_p is the weight ascribed to the damping constraints; and λ_v and λ_h are the weights ascribed to the vertical and horizontal smoothing constraints respectively. We used a jumping strategy to minimize the dependence of the solution on the initial model (Shaw and Orcutt, 1985) and limited the inversions to 5 iterations since this was always sufficient to obtain convergence.

We initially used a one-dimensional starting velocity model based on picking approximate velocities along Line 2 of Christeson et al. (2003), but in subsequent inversions, including those presented in this paper, we used a one-dimensional starting model (Fig. 5) that is a horizontal average of the structure imaged along the NNW–SSE profile to the south of the Island.

6. Results

We performed tomographic inversions along each profile with a variety of smoothing and damping weights. The images presented in Figs. 6 and 7 are our preferred two-dimensional models. The primary features in the models are relatively insensitive to the choice of inversion parameters and starting models. In addition, these features

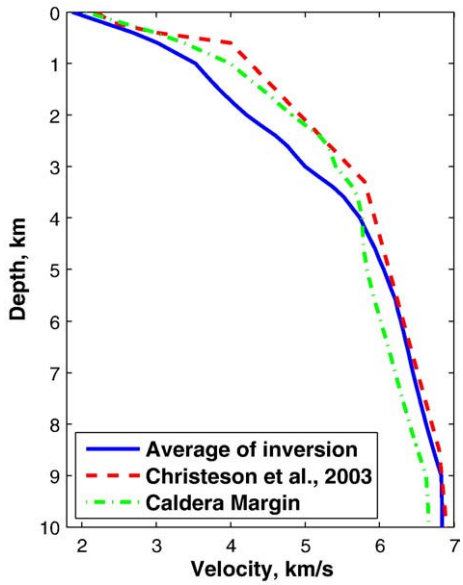

Fig. 5. Plot of one-dimensional velocity models showing the starting model for the initial inversions (dashed) that was derived from Line 2 of Christeson et al. (2003); the starting model for the inversions of field data shown in this paper (solid) which was derived by averaging the initial inversion velocities in Bransfield Strait to the south of the Island; and the velocity structure at a horizontal coordinate of 4.8 km in the NNE–SSW inversion (dot-dashed) that was used as the reference model for melt fraction calculations.

are robust, in that they are likewise reconstructed by inversions that exclude shots and stations lying near the edges of the profile corridors. Fig. 8 shows scatter plots of the travel time residuals plotted against range for each profile for the best fitting one-dimensional solution and for the preferred two-dimensional models.

6.1. NNW–SSE line

Our preferred inversion along the NNW–SSE profile (Figs. 6a and 7a) was obtained with a damping weight $\lambda_p = 1000$ and smoothing weights $\lambda_v = \lambda_h = 300$. Varying these weights by a factor of two has only a marginal effect on the appearance of the models, changing the peak magnitude of he primary low and high velocity anomalies near the volcano by at most 10–15%. The RMS travel time residual is 57 ms compared with 297 ms for the best-fitting one-dimensional model, a variance reduction of 96%. The normalized chi-squared value is 6.3. The ray coverage extends down to ~9 km with a high density of crossing rays beneath the volcano down to over 4 km depth.

Several features are visible in the inversion (Figs. 6a and 7a). There is a low velocity anomaly beneath much of the caldera which extends from the seafloor to the bottom of the image. The maximum negative anomaly −0.7 km/s at 3.5 km depth with an anomaly of −0.6 km/s extending up to <1 km depth. The low velocity anomaly is truncated to either side by high-velocity anomalies. The maximum negative anomaly is equivalent to a velocity perturbation of 13% with respect to the starting velocity model but 20–30% relative to the high velocity regions on either side.

To the north, the high velocity anomaly extends over 20 km to the end of the profile and has a maximum magnitude of 1.6 km/s. To the south, the high velocity region is fairly narrow (~6 km wide) and partially underlies the southern margin of the caldera. Its boundary is characterized by very high velocity gradients and its maximum anomaly is 0.6 km/s. South of Deception Island there is a 30- to 40-km-wide region with generally small negative velocity anomalies. This transitions abruptly to high velocities near the southern end of the profile.

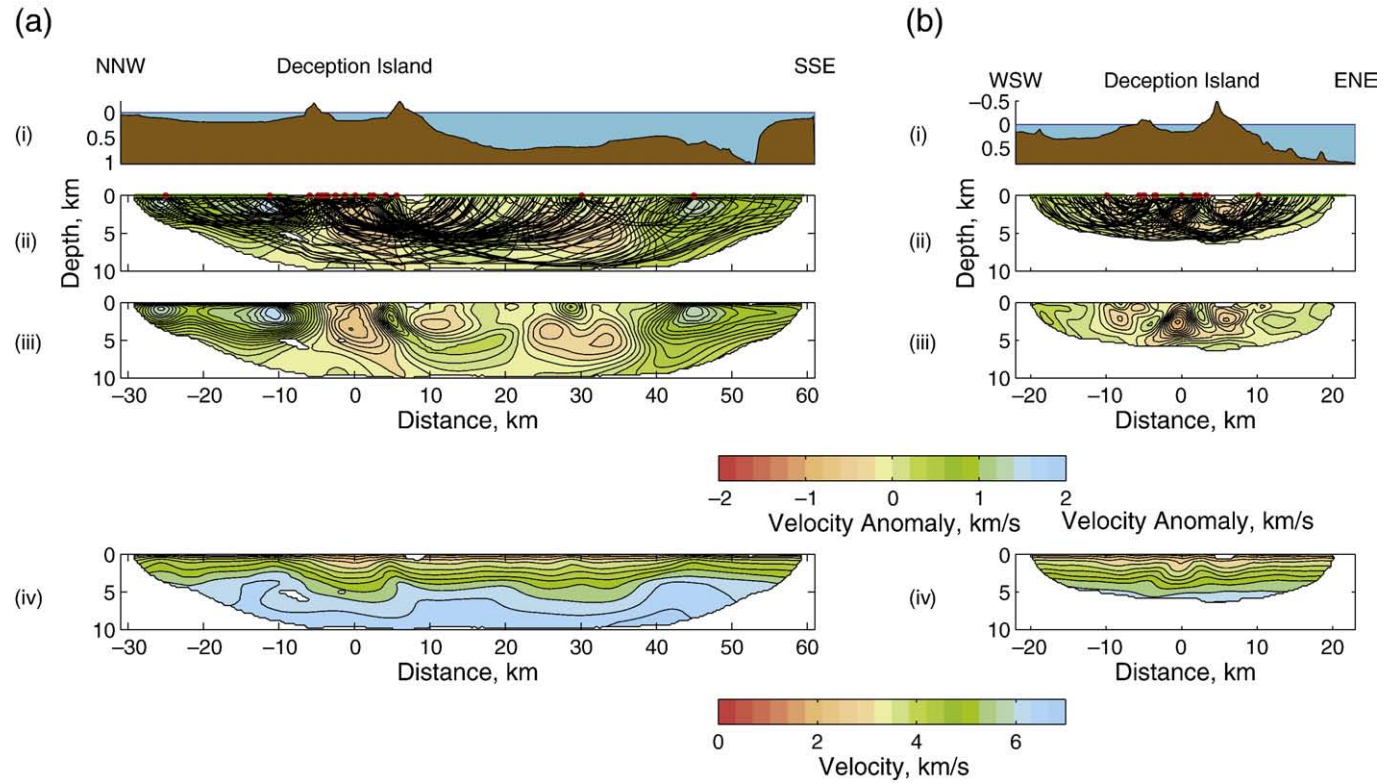

Fig. 6. (a) Results of tomographic inversions along the NNW–SSE profile showing (i) the bathymetry along the profile, (ii) the velocity perturbations overlain by every twelfth ray paths, (iii) the velocity perturbations, and (iv) the absolute velocities in the tomographic model. There is no vertical exaggeration in the middle and bottom panels. The contour interval for velocity perturbations is 0.1 km/s. The contour interval for the velocity model is 0.5 km/s. Note that tomographic model is hung from the topography/bathymetry so that depths in panels (ii)–(iv) are referenced to the elevation of the seafloor or island surface. (b) As for (a) except for the WSW–ENE profile.

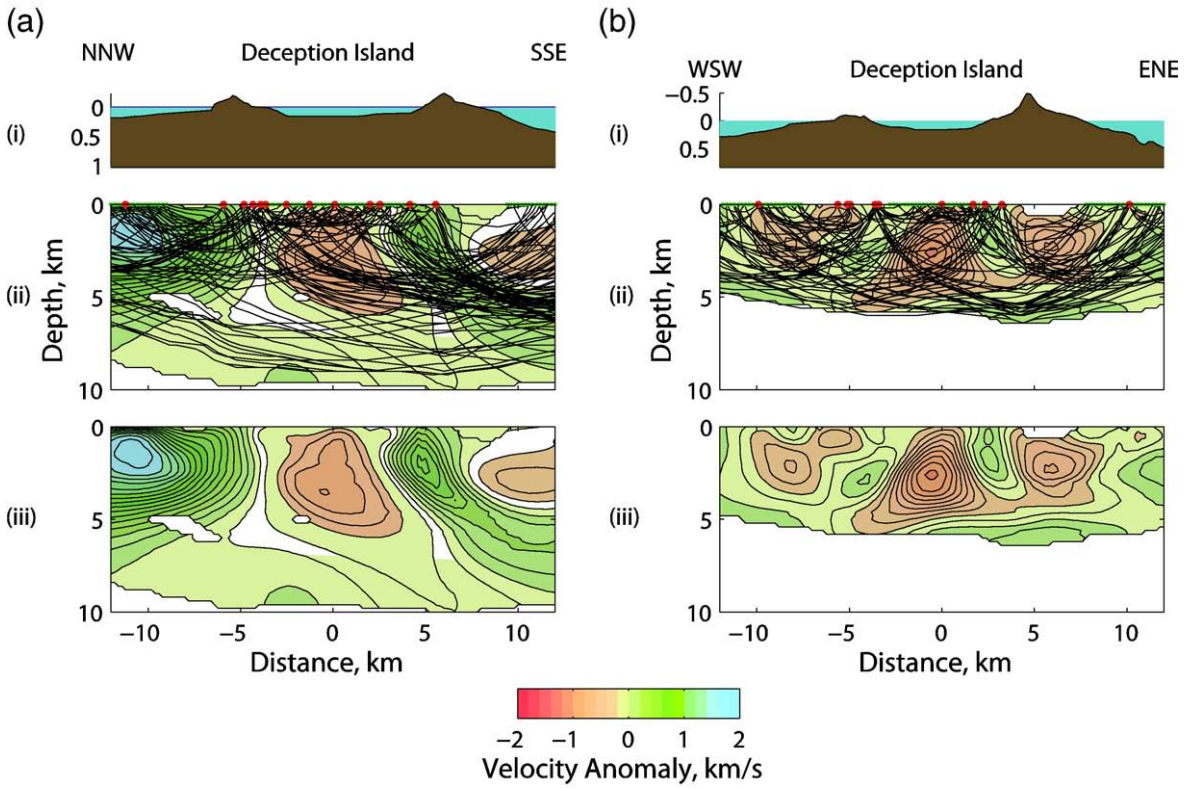

Fig. 7. As for Fig. 6 but for the region near Deception Island except that every tenth ray path is plotted and absolute velocity is not plotted.

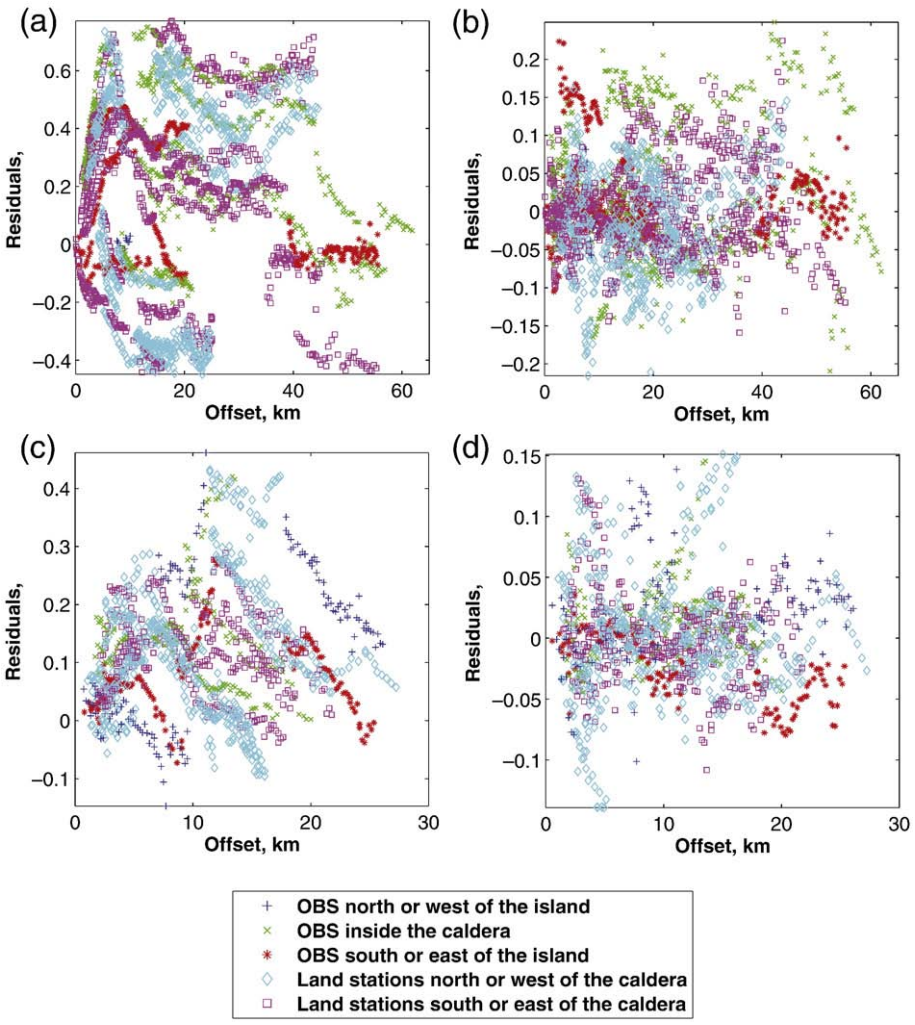

Fig. 8. Scatter plots showing travel time residuals (observed minus predicted) plotted against range with symbols differentiating between receivers in different regions. Plots are shown for (a) the best fitting one-dimensional and (b) the preferred two-dimensional model for the NNW–SSE profile and for (c) the best fitting one-dimensional and (d) the preferred two-dimensional model for the WSW–ENE profile.

6.2. ENE–WSW line

Our preferred inversion along the ENE–WSW profile (Figs. 6b and 7b) was obtained with a damping weight $\lambda_p = 1000$ and smoothing weights $\lambda_v = \lambda_h = 100$. As for the other profile the inversion is relatively insensitive to the precise choice of these parameters. The RMS travel time residual is 40 ms compared with 123 ms for the best-fitting one-dimensional model, a variance reduction of 89%. The normalized chi-squared value is 5.5. The ray coverage extends down to ~5–6 km depth with crossing rays beneath the volcano down to ~4 km (Fig. 6b). The low velocity anomaly beneath the caldera extends from the seafloor to the bottom of the image, has a width of ~4 km at shallower depths, and a minimum value of −1.0 km/s at 2.6 km depth (Fig. 7b) which is equivalent to a velocity perturbation of 20% with respect to the starting one-dimensional model. It is bounded on either side by narrow (~2 km width) high-velocity anomalies that are not as pronounced as in the NNW–ENE profile and have a maximum anomaly of ~0.2 km/s. Both flanks of the volcano are underlain by negative anomalies that extend to ~4 km depth and reach −0.5 km/s.

6.3. Checkerboard tests

We used checkerboard tests to assess the resolution of our models. For each profile, we forward modeled the travel times for the same source–receiver configuration as the data, through models comprising blocks with alternating low and high velocity anomalies of ±0.5 km/s. We then added random errors based on the assigned picking uncertainties, and inverted the synthetic data to see what features were retained. The results for both profiles show that beneath the volcano, surface blocks measuring 2 km×2 km (Fig. 9a) and 1 km×1 km are generally well resolved, but such features are not recovered at greater depths. Wider features measuring 5 km (width)×2 km (Fig. 9b) and 5 km×3 km are recovered beneath the volcano and its immediate flanks down to depths of 4 km and 6 km, respectively, but at larger depths the paucity of crossing rays substantially limits resolution. We infer that the models have limited vertical resolution at depths >~4 km.

7. Discussion

We have presented inversions for two-dimensional velocity structure along two orthogonal profiles across Deception Island volcano. The inversions only resolve features down to ~4 km depth, in part because the OBSs deployed at several sites along the profiles did not return data. At shallower depths the resolution is quite good particularly beneath the volcano and the inversions reveal considerable heterogeneity along the profiles.

Both inversions have normalized chi-squared values that are markedly greater than unity indicating that the travel time data are not fit to their

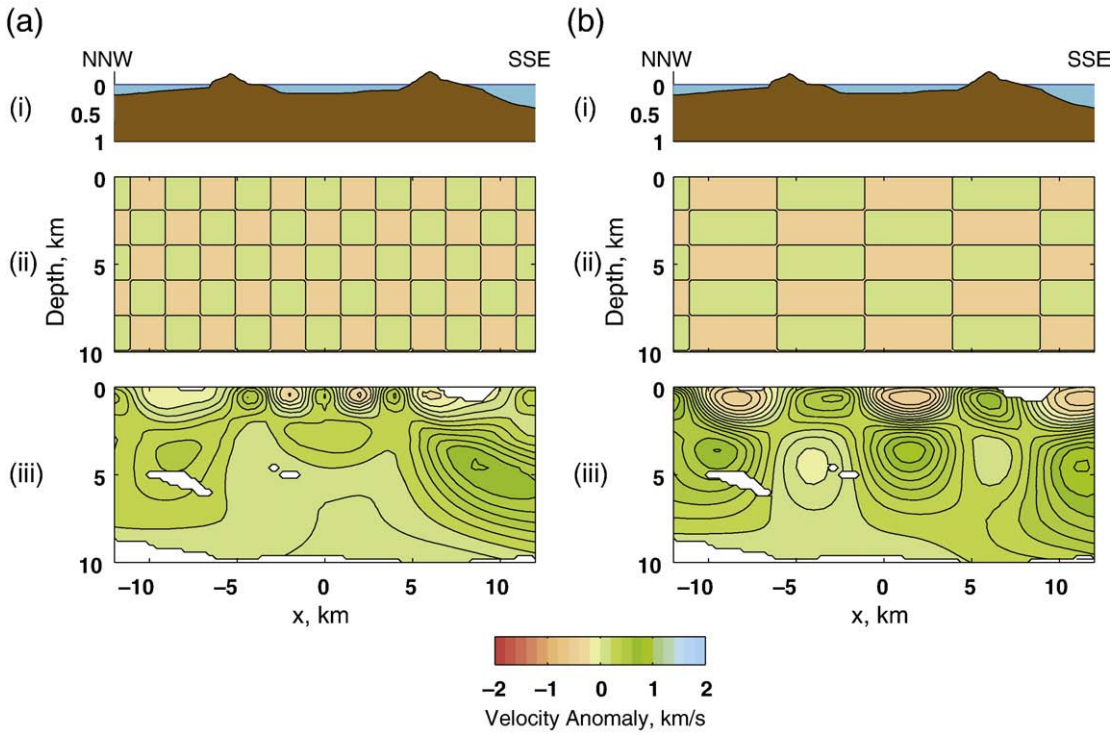

Fig. 9. (a) Result of a checkerboard test for the NNW–SSE line for blocks with dimensions of 2 km×2 km and anomalies of ±0.5 km/s showing (i) the bathymetry along the profile, (ii) the starting velocity perturbation model with the checkerboard pattern that is used to forward model travel times, and (iii) the velocity perturbations obtained from inverting the synthetic data. (b) As for (a) but for blocks with dimensions of 5 km×2 km.

nominal picking uncertainty. The maximum magnitude of the travel time residuals is ~200 ms and ~150 ms for the NNE–SSW (Fig. 8b) and WSW–ENE (Fig. 8c) inversions, respectively. It is possible that our data set includes a few mispicked first arrivals on traces with low signal to noise although we reinspected all the data with large residuals in our preliminary inversions and eliminated picks that we judged to be suspect. We have also performed inversions that iteratively excluded all observations with residuals whose magnitude is greater than 100 ms; the results are very similar to those presented her.

A more likely explanation for the high residuals is the presence of velocity variations perpendicular to the profiles. Three-dimensional inversions for shallow volcano structure (Zandomeneghi et al., 2007, submitted for publication) show significant three-dimensional within the 4- to 5-km-wide corridors used for our profiles. Because the caldera is narrower in a direction perpendicular to the NNW–SSE profile, the errors resulting from assuming a two-dimensional structure would be expected to be larger for this profile, an inference that is consistent with the observed residuals.

7.1. Structure around the Volcano

To the north of the caldera, there is a broad high-velocity anomaly that extends to the end of the profile. The region of high gradients between this high velocity anomaly and the low velocities beneath the caldera coincides with a regional normal fault that marks the northern border of extension in Bransfield Strait (Barker and Austin, 1998; Rey et al., 2002). Away from Deception Island, this fault is delineated by the steep bathymetry gradients on the northwest side of Bransfield Strait (Fig. 1). When extrapolated across Deception Island the fault coincides with the northwestern margin of the caldera and with the line of 1967 and 1970 eruption centers near Telefon Bay (Rey et al., 1997). The fault may play a role in constraining the volcano's location, although other volcanic centers in the Central Bransfield Basin are not located along the north-bounding fault (Gràcia et al., 1997). It may also provide a deep conduit that allows arc-like magma to migrate to the volcano. On the basis of the analysis of magnetic and gravimetric data, Muñoz-Martín et al. (2005) argue that this fault marks the boundary between continental crust to the north of Deception Island and more basic crust to the south. However, at the depth of imaging for our model (<~5 km), the north to south decrease in velocity across this boundary imaged by our study and previous investigations (Grad et al., 1992; Christeson et al., 2003) is more consistent with a transition from undeformed continental crust to the north to extended continental crust to the south that is overlain by sediments and volcanics.

To the west, south and east, the low-velocity anomaly beneath the caldera is flanked by a narrow zone of high velocities which transitions to a zone of low velocities further beneath the volcano flanks. The low velocity anomalies on the flanks of the volcano are likely indicative of the pillow lavas, hyaloclastic breccia, mass slumps, and tephra that were deposited during the history of the volcano (Smellie, 2002a). The narrow high-velocity anomaly is particularly prominent beneath the southern margin of the caldera (Fig. 7a) where it is not clearly related to any surface feature. It is well imaged at shallower depths but it is elongated at depth along the predominant ray path direction (Fig. 6a) suggesting that its base is not well resolved. One interpretation of this feature is that it is a cooled magmatic intrusion that penetrates to shallow depths. The high-velocity anomalies along the WSW–ENE profile (Fig. 7b) are less pronounced, particularly on the west side of the caldera, but three-dimensional inversions (Zandomeneghi et al., 2007, submitted for publication) show that there is a ring of high-velocity anomalies around the caldera that is attributed to a pre-caldera shield phase of the volcano, a previous caldera rim, or to shallow intrusions.

The broad region of low velocity anomalies located south of the island in Bransfield Strait (Fig. 6a) is presumably a region where sediments and volcanic sequences have accumulated in the extensional basin. The high velocity anomaly at the southern end of the NNW–SSE profile is somewhat puzzling. A velocity increase would be expected south of the southern margin of the basin because the sediment thickness would decrease markedly. However this anomaly lies within the basin (this is clearly apparent in the bathymetry of the profile shown in Fig. 6a). Further

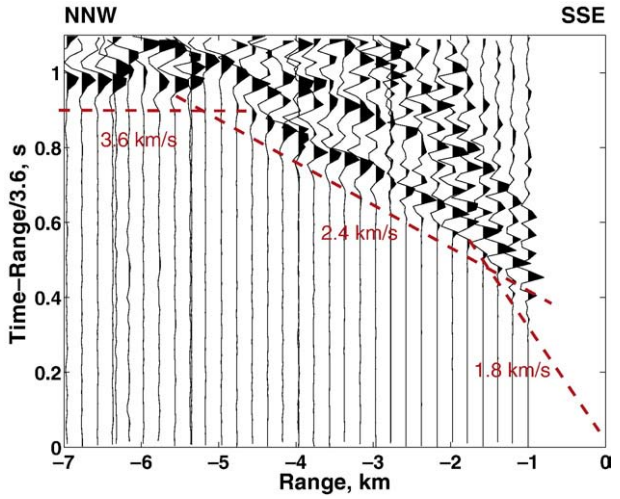

Fig. 10. Record section for shots inside the caldera recorded by Station W25 on the north shore of the caldera (the station and shot locations are shown in Fig. 14a), plotted with a reduction velocity of 3.6 km/s. A water path correction derived from the tomography code has been applied to correct the shot locations and times to the ray entry point and time at the seafloor. The data for this record section are fit well by a three layer model with two upper sediment layers with an average velocity of 2.1 km/s and a total thickness of 1.2 km overlying a basement layer with velocities of 3.6 km/s.

east Barker and Austin (1998) found evidence for magmatic intrusions near the southern margin of the basin and such an explanation would be consistent with high seismic velocities we resolve. The high velocity feature might also be related to the segmentation of the Bransfield Basin across northwest–southeast trending structures (Christeson et al., 2003). Finally, it is possible that the steep bathymetry observed near the southern end of the profile has affected the accuracy of the travel time calculations for the water paths.

7.2. Origin of the low-velocity anomaly beneath the caldera

In order to understand the origin of the low velocity anomaly beneath the caldera, we first sought to assess the contribution from shallow sediments and unconsolidated volcanics. Refraction profiles within the caldera (Fig. 10), many of which are reversed, are fit well by a layered model in which a lower layer with velocities of 3.5–4 km/s that we interpret as basement that is overlain by a 1.2-km-thick region that can be approximated by two layers with an average velocity of ~2.1 km/s which we interpret as sediments and pyroclastics. These results are very consistent with an earlier study (Grad et al., 1992).

We conducted synthetic inversions that were based on travel times obtained by ray tracing for the same source and receiver geometry as for our field data through a velocity model in which a 1.2-km-thick sediment layer in the caldera region was superimposed on a one-dimensional starting model (Fig. 11a). As might be anticipated from the checkerboard tests, the inversion results show that the sediment basin is well resolved and does not smear out in the images to larger depths. We infer that it contributes very little to the low velocity anomaly at depths >1.5–2 km and that only a small proportion of the observed low-velocity anomaly is the result of this layer.

We cannot entirely discount the possibility that the sediments and pyroclastic layers extend below 1.2 km depth (Grad et al., 1992). The large velocity jump inferred from the refraction data is most easily explained by a lithological boundary, but it is also possible that a highly fractured or porous region in the uppermost basement contributes to the low velocity anomaly. To investigate this idea, we obtained a second synthetic inversion with 2-km-thick "sediment" layer. The inversion shows more smearing but still does not reproduce the low-velocity anomaly recovered from the field data (Fig. 7a) at depth below ~3 km. We infer that even a substantially thicker sediment basin or a sediment basin underlain by a layer of fractured basement cannot account for the full depth of the low velocity anomaly.

To explore the hypothesis that the 1.2-km-thick layer of sediments and pyroclastics is underlain by a shallow magma chamber we systematically investigated synthetic models that included both the caldera sediments and an underlying magma chamber of varying dimensions and anomaly size. Fig. 12a shows one example of a synthetic test for the NNW–SSE profile. The synthetic

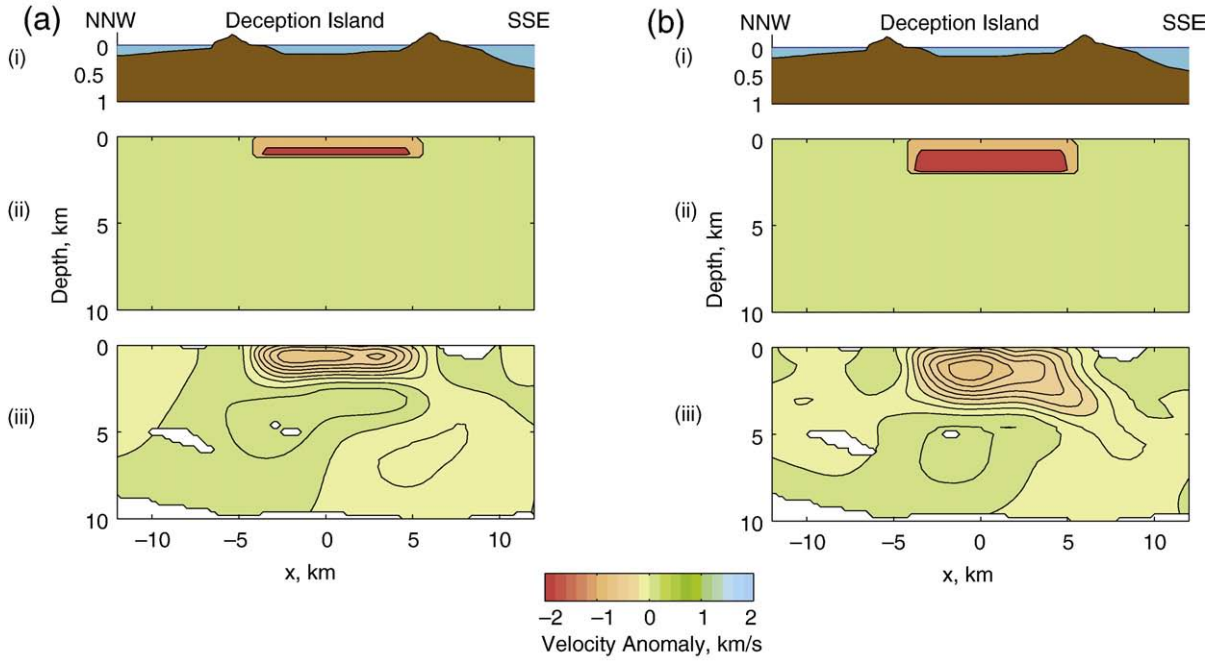

Fig. 11. Results of a synthetic inversions along the NNW–SSE profile based on forward modeling travel times through caldera sediment basins with uniform velocities of 2.1 km/s superimposed on the one-dimensional starting model. (a) An inversion for a 1.2-km-thick sediment basin with panels showing (i) the bathymetry along the profile, (ii) the velocity perturbations for starting model used for forward modeling, (iii) the velocity perturbations obtained from the inversion. (b) As for (a) except for a 2-km-thick sediment basin.

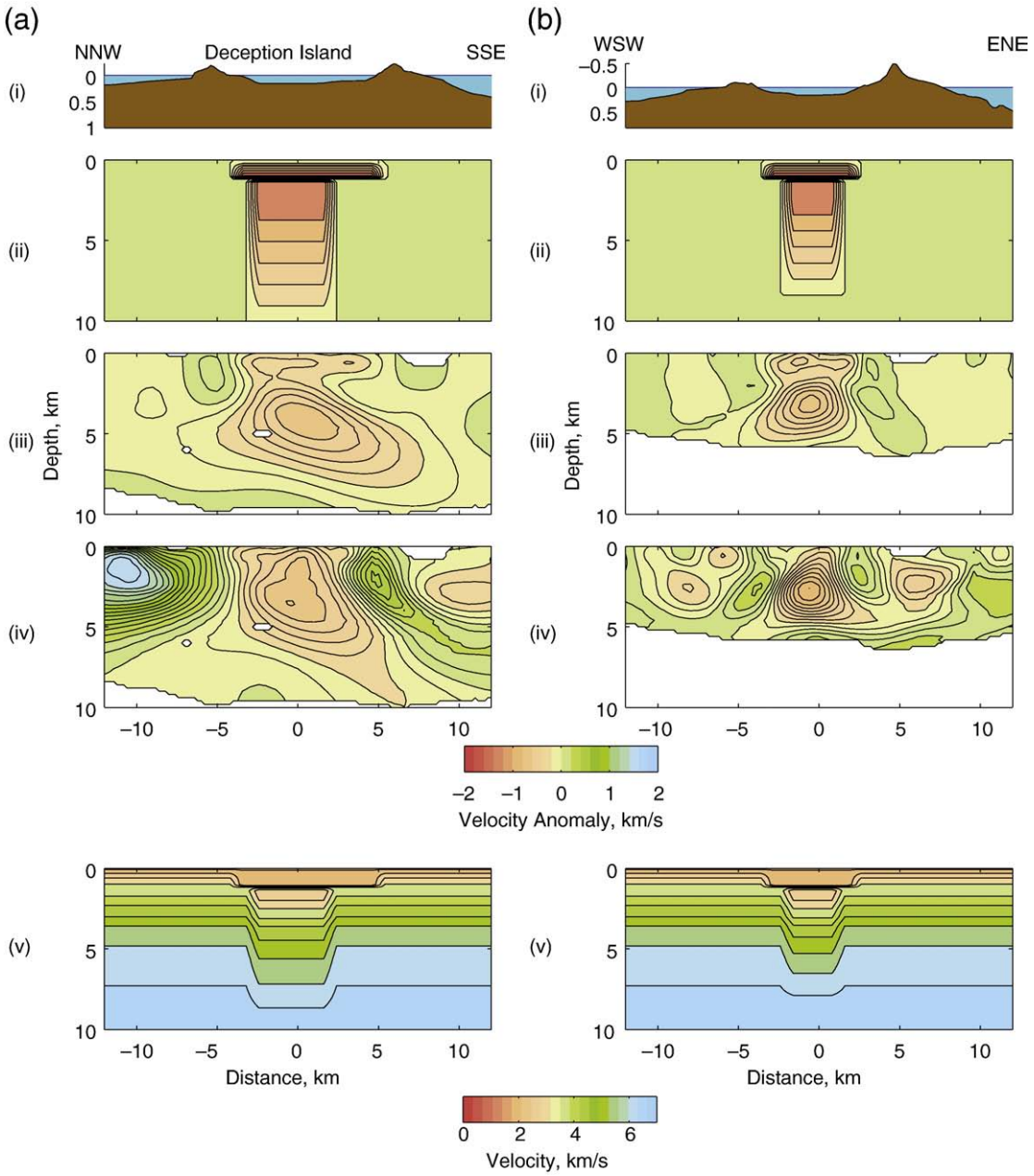

Fig. 12. (a) Results of a synthetic inversion for the NNW–SSE profile based on forward modeling travel times through a model that includes the caldera sediment basin and an underlying magma chamber. The magma chamber is 4.8 km wide and extends downward from 1.5 km depth with a velocity anomaly of −1.2 km/s in its upper 2 km that decreases linearly at greater depth to zero at 10 km depth. The panels are as follows: (i)–(iii) as for Fig. 11, (iv) the velocity perturbations for inverting the field data for comparison (from Figs. 6 and 7), and (v) the absolute velocities for starting model used for forward modeling travel times for the synthetic inversion. (b) As for (a) except for the WSW–ENE line and with a magma chamber that is 3 km wide.

model includes a 4.8-km-wide magma chamber that extends downwards from a depth of 1.4 km and has an anomaly which is −1.2 km/s in its upper 2.0 km and then decreases linearly downwards to zero at 10 km depth. The synthetic inversion results in a low-velocity anomaly that is somewhat wider than recovered from the inversions of the field data (Fig. 7a) which may be because the starting model for the synthetic inversion does not include the high velocity regions on either side that are recovered in the inversions of the field data. Otherwise, it reproduces the basic characteristics of the observed anomaly quite well. Fig. 12b shows a similar synthetic inversion for the ENE–WSW line for a starting model with a magma chamber that has a width of 3 km that approximately matches the low velocity anomaly recovered from the real data. Based on such tests we infer that the top of the magma chamber is likely at ≤2 km depth, and that its width is between 3 and 5 km along the NNW–SSE profile and 2–3 km along the ENE–WSW profile. To reproduce the amplitude of the velocity anomalies seen in the field data inversions, a velocity anomaly of −1.2 to −1.5 km/s (25–40%) is required in the synthetic models. The base of the magma chamber is not resolved but the synthetic inversions suggest that a significant velocity anomaly must extend to >4 km depth in order to match the depth of the anomaly seen in the field data inversions.

7.3. Estimates of melt volumes

In order to estimate the melt content of the possible magma chamber, we applied a method that is described in detail by Dunn et al. (2000). The first step involves estimating the velocity anomaly that can

be attributed to elevated subsolidus temperatures. Karato (1993) presents an equation for the sensitivity of velocity to temperature

$$\frac{d\ln V}{dT} = \frac{d\ln V}{dT}\bigg|_{\text{anharmonic}} - F(\alpha)\frac{Q(f,T)^{-1}}{\pi}\frac{H^*}{RT}$$

where V is the P-wave velocity, T is the temperature, a is exponential frequency-dependence of Q, $F(\alpha)$ has a value near 1, f is frequency, H^* is an activation enthalpy, and R is the gas constant. The two terms on the right hand side are the anharmonic term which involves no energy loss and anelastic term which is associated with attenuation and is frequency dependent. There is significant uncertainty in the parameter values that control the anelastic term. Dunn et al. (2000) choose to estimate the upper and lower bounds of the subsolidus temperature contribution by considering, respectively, only the anharmonic term and the sum of the anharmonic and anelastic term with parameter values for the latter chosen to maximize the anelastic contribution.

Since Deception Island has a composition that is close to basaltic, we use the same parameter values that Dunn et al. (2000) use for the oceanic crust. We assume a uniform $Q_P = 50$, a value that is higher than near surface values estimated at Deception Island from earthquake records using pulse broadening and a spectral technique (Martinez-Arévalo et al., 2003), but a reasonable lower-bound on average values for the upper 5 km based on attenuation studies at other volcanoes (e.g., Wilcock et al., 1995; Giampiccolo et al., 2007). We estimated the velocity anomalies as a function of temperature perturbation using a background temperature model that increases linearly from 0 °C at the seafloor to a solidus temperature of 1050 °C at 15 km depth, the crustal thickness inferred by Christeson et al. (2003). This leads to a cross-section of apparent crustal temperatures (Fig. 13a) that in some models delineates a region where the velocity anomaly cannot be entirely accounted for by sub-solidus temperatures.

The second step of the method involves interpreting the unexplained component of the anomaly in terms of melt fraction using a theoretical model developed by Schmeling (1985). Following Dunn et al. (2000) we consider melt aspect ratios of 0.05 and 1.0 to obtain lower and upper bounds on the melt fraction at each location where temperature cannot account for the whole velocity anomaly (Fig. 12b and c). The cross sections of melt fraction can be integrated to obtain an equivalent melt area. We limit this integration to regions lying beneath the sediment layer, and to a maximum depth of 5 km.

The technique is sensitive to the reference one-dimensional velocity model used to estimate the velocity anomaly. The starting velocity model for our inversions (Fig. 5) and the reference model for plotting anomalies is based on the one-dimensional structure in the basin away from the Island and the velocities are almost certainly too low for a basaltic-andesite volcano. The model we obtained from Christeson et al. (2003) has markedly higher velocities in the upper 4 km (Fig. 5). However, rather than using either of these models we

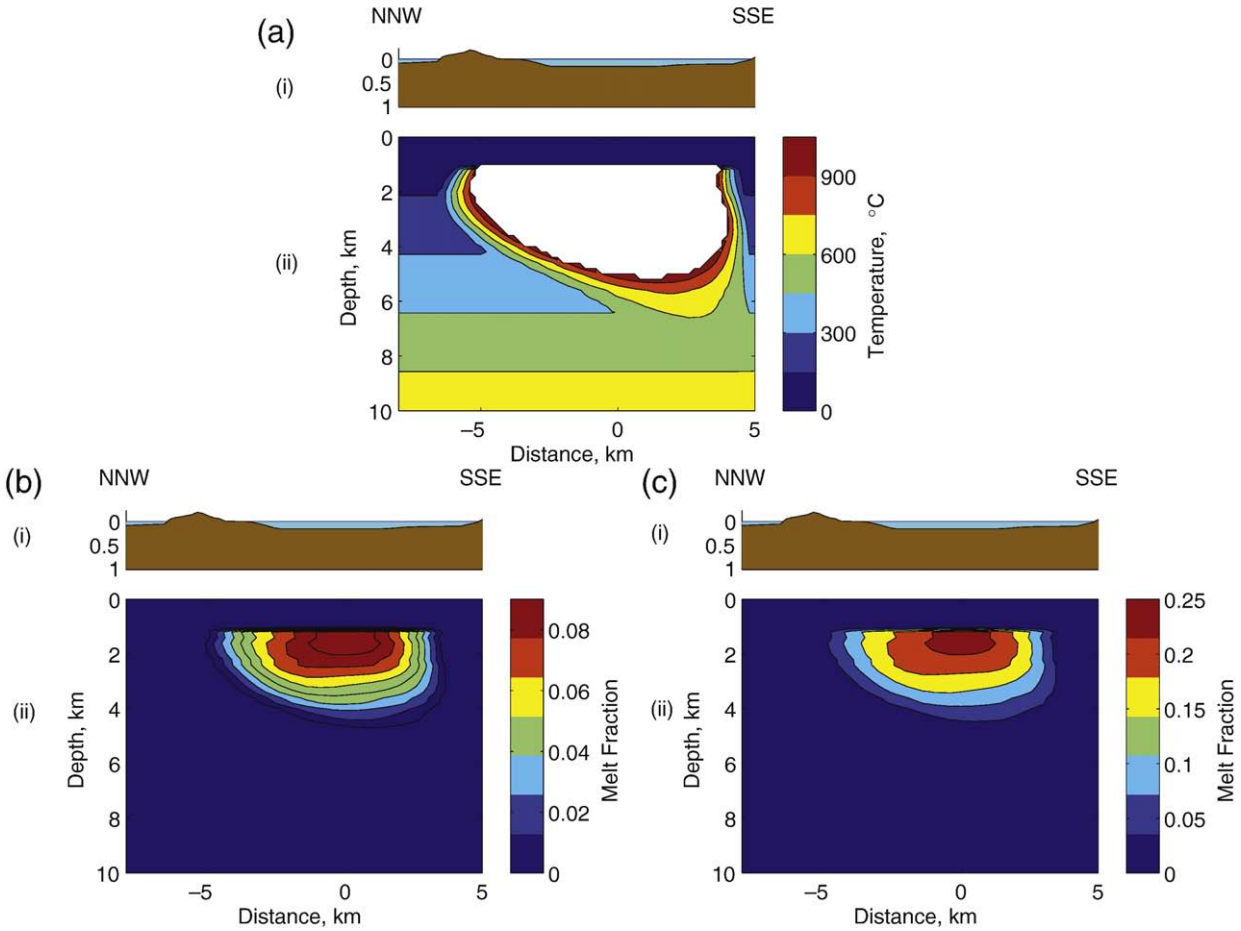

Fig. 13. Example of melt calculations using the method of Dunn et al. (2000) (a) Temperatures calculated from seismic velocity anomaly in the vicinity of the island along the NNW–SSE profile assuming only the anharmonic term (see text). The bathymetry along the profile is underlain by a contour plot of the calculated temperature anomaly. White shading indicates a region where the temperatures exceed the solidus temperature of 1050 °C. Note that temperature anomalies are not calculated for the upper 1.2 km since this corresponds to the sediment basin. (b) Melt fractions calculated from the excess negative velocity anomalies using the model of Schmeling (1985) and a melt pocket aspect ratio of 0.05. (c) As for (b) except for a melt pocket aspect ratio of 1.0.

Table 1
Estimates of melt bounds in the Deception Island magma chamber obtained with the method of Dunn et al. (2000)

Inversion	Anharmonic						Anelastic and anharmonic					
	Melt AR=0.05			Melt AR=1.0			Melt AR=0.05			Melt AR=1.0		
	Max. melt, %	Melt area, km^2	Melt vol., km^3	Max. melt, %	Melt area, km^2	Melt vol., km^3	Max. melt, %	Melt area, km^2	Melt vol., km^3	Max. melt, %	Melt area, km^2	Melt vol., km^3
NNE–SSW field data (Fig. 7a)	12	1.6	4.9	33	4.5	14	0	0.0	0.0	0	0.0	0.0
WSW–ENE field data (Fig. 7b)	13	1.5	7.3	38	4.1	20	0	0.0	0.0	0	0.0	0.0
NNE–SSW synthetic (Fig. 12a)	16	2.4	7.3	48	6.9	21	5	0.3	0.8	13	0.8	2.3
WSW–ENE synthetic (Fig. 12b)	16	1.5	7.5	48	4.3	21	5	0.2	0.9	13	0.5	2.4

These calculations are described in the text. The melt areas are based on integrating melt fractions down to 5 km depth and the melt volumes are obtained by multiplying the melt areas by 3 km and 5 km for the NNE–SSW and WSW–ENE profiles, respectively. Melt AR stands for the aspect ratio of melt pockets.

chose to estimate the velocity anomaly with respect to the highest velocities imaged in the high-velocity region to the south of the volcano center (a horizontal coordinate of 4.8 km in Fig. 7a) since all the explanations of this feature envision that it is composed of solid volcanic material (Zandomeneghi et al., 2007, submitted for publication). This model is shown in Fig. 5 and is intermediate between the other two velocity models at shallower depths.

Table 1 summarizes the results of melt calculations that have been applied to both the inversions of the field data and the starting models for the synthetic magma chamber inversions. The results for the field data give bounds on the maximum melt fraction ranging from 0 to nearly 40% with a simple estimate of the melt volume ranging from 0 to 14–20 km^3. The wide bounds on the melt content illustrate the difficulties associated with such calculations (e.g., Lees, 2007). Further uncertainties will arise from the choice of reference velocity and temperature model. Because of the tendency for inversions to smear out features, the velocity difference associated with the anomaly is almost certainly underestimated. We also note that the theoretical models of Schmeling (1985) are only presented for relatively small melt fractions (<~15%) and their extrapolation almost certainly overestimates the effect of larger melt fractions on velocity. Both these factors would lead to underestimates of melt fractions and volumes.

It is interesting to note that the synthetic starting models that reproduce that low-velocity anomaly observed in the inversions increase from 2.6 to 3.0 km/s over the upper 1 km anomaly (Fig. 12, bottom panels). Such velocities suggest basaltic or andesitic melt contents approaching or reaching 100% (Murase and McBirney, 1973) and are thus consistent with melt volumes of up to 15 km^3. While our

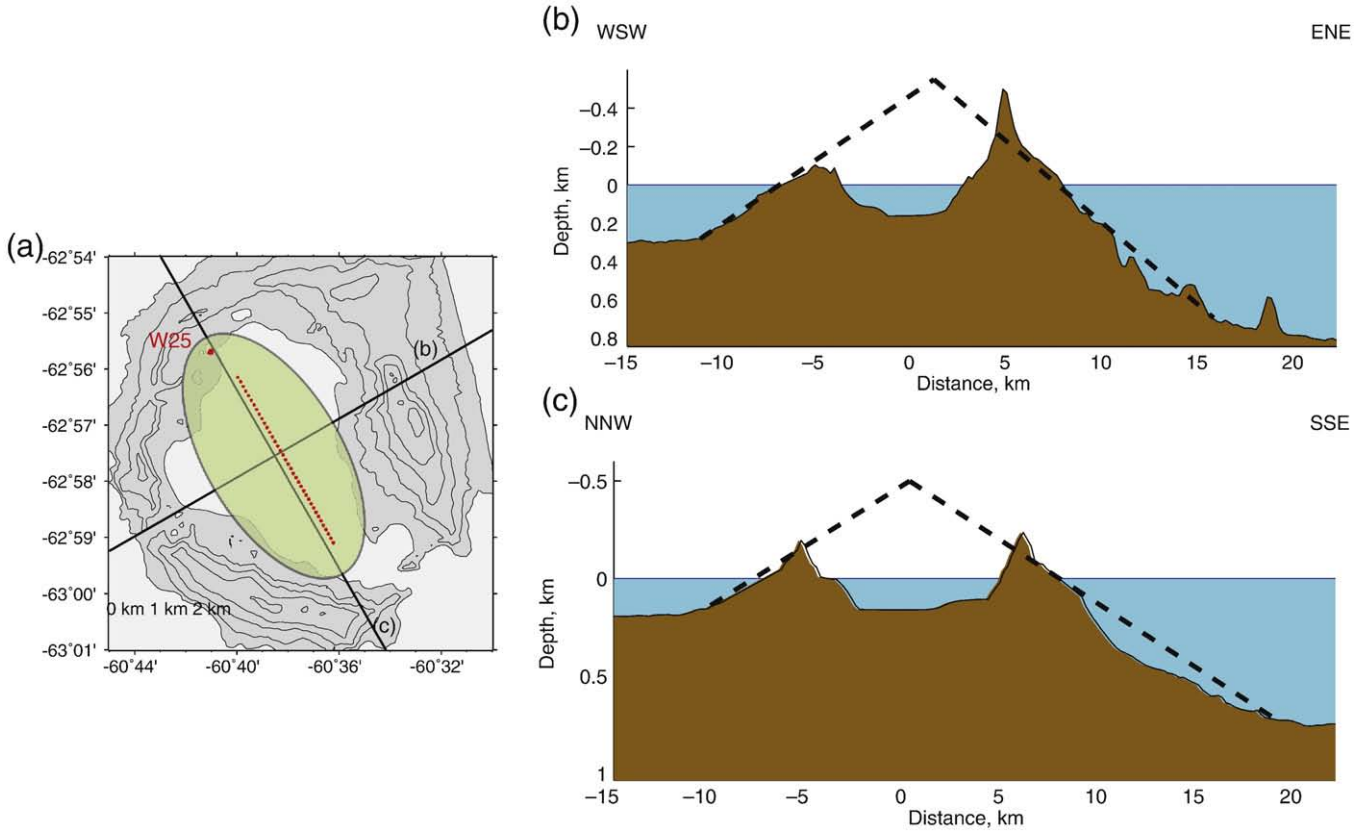

Fig. 14. (a) Map of the Deception Island showing that the caldera can be approximated by an ellipse with semi-axes measuring 4.5 km and 2.7 km. The square labeled W25 and the line of dots show and receiver and shot line for the record section shown in Fig. 10. Solid lines show the locations of the cross-sections shown in (b)–(c). (b) WSW–ENW cross-section of Deception Island with a vertical exaggeration of 10 showing an assumed conical shape of the volcano prior to the caldera forming eruption(s). (c) As for (b) except for an NNW–SSE section. Based on our estimate of the caldera sediment basin depth, we estimate that the caldera forming eruption(s) ejected ~60 km^3 of material.

velocity inversions and synthetic models do not have the vertical resolution to demonstrate that Deception Island is underlain by a substantial volume of melt (we cannot, for instance, discount the contribution of a fractured upper basement), we infer that they are consistent with this interpretation.

7.4. Implications of a shallow magma chamber

The possible existence of a large magma chamber beneath the caldera is consistent with the recent eruptive history of Deception Island. Two unusual features of the historical eruptions are that they have occurred all around the caldera and that at least three eruptive events have included simultaneous eruptions of chemically distinct lavas from multiple vents (Newhall and Dzurisin, 1988, pp 1015). These characteristics are most simply explained if volcanism results from small differentiated magma bodies that rise up from a large magma chamber that extends across the whole caldera (Roobol, 1980).

The presence of shallow magma chamber is also consistent with the geochemistry of the volcano. Major and trace element variations require extensive fractionation at shallow crustal depths (Smellie, 2002a). Fluorine and boron systematics have led Smellie et al. (1992) to postulate that Deception Island is underlain by a shallow basaltic magma chamber that undergoes open system fractionation with the regular influx and eruption of small batches of magma.

We can use our constraints on the thickness of the caldera sediment layer to estimate the maximum volume of material that could have been ejected if the caldera formed by one or more eruptions. We approximate the caldera by an ellipse with semi-major and semi-minor axes of 4.5 km and 2.7 km, respectively, (Fig. 14a) and a thickness of 1.4 km (the thickness of the water and sediment layers) and assume that the emerged volcano had a conical shape prior to the eruption and a maximum elevation above sea level of 500 m (Fig. 13b and c). This yields a volume of ~60 km^3 which is significantly larger than the 30 km^3 estimated by Smellie (2001) but similar to an estimate of Martí et al. (1996).

The conventional view of volcanic hazard at Deception Island is that it is in the early stage of infilling the caldera by small-volume eruptions (Roobol, 1982; Smellie, 2002b). However, evidence from other volcanoes shows that small eruptions of silicic magmas around ring structures have preceded some large, prehistoric eruptions (Bacon, 1985) and so one could speculate that the recent activity at Deception may be a precursor to a much larger eruption and caldera collapse (Newhall and Dzurisin, 1988, p. 1015). Repeat bathymetric surveys (Cooper et al., 1998) are consistent with, but do not require (Barclay et al., in press), substantial resurgence on the east side of the caldera. However, seismic data suggest that the caldera has undergone several episodes of trap-door deformation (Cooper et al., 1998) and these were not accompanied by large eruptions (Smellie, 2001). It has been postulated that the caldera forming eruption was triggered by the influx of a second compositionally different magma (Smellie et al., 1992; Smellie, 2001). Thus, while the possible presence of a sizeable shallow magma chamber beneath Deception Island may indicate that the volcano could support a large eruption, it might require an additional triggering event (Smellie, 2001).

8. Conclusions

We have presented two-dimensional inversions for P-wave velocity structure along two orthogonal profiles across Deception Island. The primary conclusions of this study are:

1. There is a substantial increase in velocities across a regional normal fault that marks the northwestern margin of the Bransfield Basin and which coincides with the northern margin of the caldera.
2. There is a significant low velocity anomaly beneath the volcano. This results from the combination of a layer of low-velocity material that infills the caldera basin and an underlying possible magma chamber that extend downwards from ≤2 km below the seafloor to >4 km depth that may contain a substantial volume of melt.
3. Formal estimates of the melt volume in the magma chamber region obtained using a method described by Dunn et al. (2000) range from 0 to 20 km^3. The presence of a large shallow magma chamber is thus not required by our data but is consistent with the absolute velocities inferred from synthetic inversions. It is also consistent with the distribution and timing of recent eruptions and with the petrology of basalts.

Acknowledgements

We thank the officers and crew of the R/V *Hespérides* and *R/V Las Palmas*, the personnel of the Gabriel de Castilla base, and the members of the TOMODEC Working Group for their assistance with this experiment and two anonymous referees for detailed reviews. This work was supported by US National Science Foundation grant ANT-0230094 and Spanish Institute of Science and Technology grant REN 200-3833.

References

Bacon, C.R., 1985. Implications of silicic vent patterns for the presence of large crustal magma chambers. J. Geophys. Res. 90 (B13), 11243–11252.
Baker, P.E., McReath, I., Harvey, M.R., Roobol, M.J., Davis, T.G., 1975. The Geology of the South Shetland Islands: V. Volcanic Evolution of Deception Island. British Antarctic Survey Scientific Reports, vol. 78. 81 pp.
Barclay, A.H., Wilcock, W.S.D. and Ibáñez, J.M., in press. Bathymetric Constraints on the Tectonic and Volcanic Evolution of Deception Island Volcano, South Shetland Islands. Antarctic Science. doi:10.1017/S0954102008001673.
Barker, P.F., 1982. The Cenozoic subduction history of the Pacific margin of the Antarctic Peninsula: ridge crest–trench interactions. J. Geol. Soc. Lond. 139, 787–801.
Barker, D.H.N., Austin, J.A., 1998. Rift propagation, detachment faulting, and associated magmatism in Bransfield Strait, Antarctic Peninsula. J. Geophys. Res 103 (B10), 24017–24044.
Chiarabba, C., Moretti, M., 2006. An insight into the unrest phenomena at the Campi Flegrei caldera from V_P and V_P/V_S tomography. Terra Nova 18, 373–379.
Christeson, G.L., Barker, D.H.N., Austin, J.A., Dalziel, I.W.D., 2003. Deep crustal structure of Bransfield Strait: initiation of a back arc basin by rift reactivation and propagation. J. Geophys. Res. 108 (B10), 2492. doi:10.1029/2003JB002468.
Cooper, A.P.R., Smellie, J.L., Maylin, J., 1998. Evidence for shallowing and uplift from bathymetric records of Deception Island, Antarctica. Antarct. Sci. 10, 455–461.
Detrick, R.S., et al., 1987. Multi-channel seismic imaging of a crustal magma chamber along the East Pacific Rise. Nature 326, 35–41.
Dunn, R.A., Toomey, D.R., Solomon, S.C., 2000. Three-dimensional seismic structure and physical properties of the crust and shallow mantle beneath the East Pacific Rise at 9°30′N. J. Geophys. Res. 105, 23537–23555.
Einarsson, P., 1978. S-wave shadows in the Krafla caldera in NE-Iceland, evidence for a magma chamber in the crust. Bull. Volcanol. 41–3, 187–195.
Finlayson, D.M., Gudmundsson, O., Itikarai, I., Nishimura, Y., Shimamura, H., 2003. Rabaul Volcano, Papua New Guinea: seismic tomographic imaging of an active caldera. J. Volcanol. Geotherm. Res. 124 (3–4), 153–171.
Giampiccolo, E., D'Amico, S., Patané, D., Gresta, S., 2007. Attenuation and source parameters of shallow microearthquakes at Mt. Etna volcano, Italy. Bull. Seismol. Soc. Am. 97, 184–197.
Gràcia, E., Canals, M., Farrán, M.-L., Sorribas, J., Pallàs, R., 1997. Central and eastern Bransfield basins (Antarctica) from high-resolution swath-bathymetry data. Antarct. Sci. 9, 168–180.
Grad, M., Guterch, A., Sroda, P., 1992. Upper crustal structure of Deception Island area, Bransfield Strait, West Antarctica. Antarct. Sci. 4 (4), 469–476.
Grad, M., Shiobara, H., Janik, T., Guterch, A., Shimamura, H., 1997. Crustal model of the Bransfield Rift, West Antarctica, from detailed OBS refraction experiments. Geophys. J. Int. 130 (2), 506–518.
Horiuchi, S., Tsumura, N., Hasegawa, A., 1997. Mapping of a magma reservoir beneath Nikko-Shirane volcano in northern Kanto, Japan, from travel time and seismogram shape anomalies. J. Geophys. Res. 102, 18,071–18,090.
Hussenoeder, S.A., Collins, J.A., Kent, G.M., Detrick, R.S., TERA Group, 1996. Seismic analysis of the axial magma chamber reflector along the southern East Pacific Rise from conventional reflection profiling. J. Geophys. Res. 101, 22,087–22,105.
Ibáñez, J.M., Almendros, J., Carmona, E., Martnez-Arevalo, C., Abril, M., 2003. The recent seismo-volcanic activity at Deception Island volcano. Deep Sea Res. II 50 (10), 1611–1629.
Iyer, H.M., 1992. Seismological detection and delineation of magma chambers: present status and emphasis on the Western USA. In: Gasparini, P., Scarpa, R., Aki, K. (Eds.), Volcanic Seismology. Springer-Verlag, New York, NY, pp. 299–338.
Iyer, H.M., Dawson, P.B., 1993. Imaging volcanoes using teleseismic tomography. In: Iyer, H.M., Hirahara, K. (Eds.), Seismic Tomography: Theory and Practice. Chapman & Hall, London, UK, pp. 466–492.

Janik, T., Sroda, P., Grad, M., Guterch, A., 2006. Moho depth along the Antarctic Peninsula and crustal structure across the landward projection of the Hero fracture zone. In: Fuetterer Dieter, K., Damaske, D., Kleinschmidt, G., Miller, H., Tessensohn, F. (Eds.), Antarctica; Contributions to Global Earth Sciences; Proceedings. Springer-Verlag, Berlin-Heidelberg, Germany.

Karato, S.-I., 1993. Importance of anelasticity in the interpretation of seismic tomography. Geophys. Res. Lett. 20, 1623–1626.

Keller, R.A., Fisk, M.R., White, W.M., 1991a. Geochemistry of Quaternary volcanism in the Bransfield Strait and South Shetland Islands: preliminary results. Antarct. J. U.S. 26 (5), 132–133.

Keller, R.A., Fisk, M.R., White, W.M., Birkenmajer, K., 1991b. Isotopic and trace element constraints on mixing and melting models of marginal basin volcanism, Bransfield Strait, Antarctica. Earth Planet. Sci. Lett. 111, 287–303.

Keller, R.A., Fisk, M.R., Smellie, J.L., Strelin, J.A., Lawver, L.A., 2002. Geochemistry of back arc basin volcanism in Bransfield Strait, Antarctica: subducted contributions and along-axis variations. J. Geophys. Res. 107 (B8), 2171. doi:10.1029/2001JB000444.

Kent, G.M., Harding, A.J., Orcutt, J.A., 1990. Evidence for a smaller magma chamber beneath the East Pacific Rise at 9o30′ N. Nature 344, 650–653.

Klepeis, R.A., Lawver, L.A., 1996. Tectonics of the Antarctic-Scotia plate boundary near Elephant and Clarence Islands, West Antarctica. J. Geophys. Res. 101, 20,211–20,231.

Larter, R.D., Henniet, J.P., Bialas, J., Meissner, R., 1991. Preliminary results of seismic reflection investigations and associated geophysical studies in the area of the Antarctic Peninsula; discussion and reply. Antarct. Sci. 3 (2), 217–222.

Lees, J.M., 2007. Seismic tomography of magmatic systems. J. Volcanol. Geotherm. Res. 167, 37–56.

Lutter, W.J., et al., 1995. Teleseismic P-wave image of crust and upper mantle structure beneath the Valles caldera, New Mexico: initial results from the 1993 JTEX passive array. Geophys. Res. Lett. 22, 505–508.

Maestro, A., Somoza, L., Rey, J., Martínez-Frías, J., López-Martínez, J., 2007. Active tectonics, fault patterns, and stress field of Deception Island: a response to oblique convergence between the Pacific and Antarctic plates. J. South Am. Earth Sci. 23, 256–268.

Marsh, B.D., 1989. Magma chambers. Ann. Rev. Earth. Planet. Sci. 17, 439–474.

Martí, J., Vila, J., Rey, J., 1996. Deception Island (Bransfield Strait, Antarctica); an example of a volcanic caldera developed by extensional tectonics. In: McGuire, W.J., Jones, A.P., Neuberg, J. (Eds.), Volcano Instability on the Earth and Other Planets. Geological Society Special Publications. Geological Society of London, London, UK, pp. 253–265.

Martinez-Arévalo, C., Blanco, F., Ibáñez, J.M., Del Pezzo, E., 2003. Shallow seismic attenuation and shear-wave splitting in the short period range of Deception Island volcano, Antarctica. J. Volcanol. Geotherm. Res. 128, 89–113.

Masturyono, et al., 2001. Distribution of magma beneath the Toba caldera complex, north Sumatra, Indonesia, constrained by three-dimensional P wave velocities, seismicity, and gravity data. Geochem. Geophys. Geosyst. 2 paper number 2000GC000096.

Matumoto, T., 1971. Seismic body waves observed in the vicinity of Mount Katmai, Alaska, and evidence for the existence of molten chambers. Geol. Soc. Am. Bull. 82, 2905–2920.

Miller, D.S., Smith, R.B., 1999. P and S velocity structure of the Yellowstone volcanic field from local earthquake and controlled-source tomography. J. Geophys. Res. 104, 15,105–15,121.

Mizoue, M., Nakamura, I., Yokata, T., 1982. Mapping of an unusual crustal discontinuity by microearthquake reflections in the earthquake swarm area near Ashio, northwestern part of Tochigi Prefecture, Central Japan. Bull. Earthquake Res. Inst. Univ. Tokyo 57, 653–686.

Moser, T.J., 1991. Shortest path calculation of seismic rays. Geophysics 56, 59–67.

Muñoz-Martín, A., Catalán, M., Martín-Dávila, J., Carbo, A., 2005. Upper crustal structure of Deception Island area (Bransfield Strait, Antarctica) from gravity and magnetic modelling. Antarct. Sci. 17 (2), 213–224.

Murase, T., McBirney, A.R., 1973. Properties of some common igneous rocks and their melts at high temperatures. Geol. Soc. Am. Bull. 84, 3563–3592.

Newhall, C.G., Dzurisin, D., 1988. Historical unrest at large calderas of the world. U.S. Geol. Surv. Bull. 1855.

Ortiz, R., et al., 1992. Geophysical features of Deception Island. In: Yoshida, Y., Kaminuma, K., Shiraishi, K. (Eds.), Recent Progress in Antarctic Earth Science. Terra Scientific Publishing Company, Tokyo, pp. 143–152.

Rey, J., Somoza, L., Martinez, F.J., Benito, R., Martin, A.S., 1997. Deception Island (Antarctica); a new target for exploration of Fe–Mn mineralization? In: Nicholson, K., Hein James, R., Buehn, B., Dasgupta, S. (Eds.), Manganese Mineralization; Geochemistry and Mineralogy of Terrestrial and Marine Deposits. Geological Society Special Publications. Geological Society of London, London, UK, pp. 239–251.

Rey, J., Maestro, A., Somoza, L., Smellie, J.L., 2002. Submarine morphology and seismic stratigraphy of Port Foster. In: Smellie, J.L., et al. (Ed.), Geology and Geomorphology of Deception Island. British Antarctic Survey, Cambridge, UK, pp. 40–46.

Robertson, S.D., Wiens, D.A., Shore, P.J., Smith, G.P., Vera, E., 2002. Seismicity and tectonics of the South Shetland Islands and Bransfield Strait from the SEPA broadband seismograph deployment. In: Gamble John, A., Skinner David, N.B., Henrys Stuart, A. (Eds.), Antarctica at the Close of a Millennium; Proceedings of the 8th International Symposium on Antarctic Earth Sciences. The Royal Society of New Zealand, Wellington, New Zealand.

Roobol, M.J., 1980. A model for the eruptive mechanism of Deception Island from 1820 to 1970. Bull. -Br. Antarct. Surv. 49, 137–156.

Roobol, M.J., 1982. The volcanic hazard at Deception Island, South Shetland Islands. Bull. -Br. Antarct. Surv. 51, 237–245.

Sanders, C.O., 1993. Local earthquake tomography: attenuation — theory and results. In: Iyer, H.M., Hirahara, K. (Eds.), Seismic Tomography: Theory and Practice. Chapman & Hall, London, UK, pp. 676–694.

Sanders, C., Ho-Liu, P., Rinn, D., Kanamori, H., 1988. Anomalous shear wave attenuation in the shallow crust beneath Coso volcanic region, California. J. Geophys. Res. 93, 3321–3338.

Sanford, A.R., et al., 1977. Geophysical evidence for a magma body in the vicinity of Socorro, New Mexico. In: Heacock, J.G. (Ed.), The Earth's Crust: Its Nature and Physical Properties. American Geophysical Monography, vol. 20. AGU, Washington, DC, pp. 385–404.

Schmeling, H., 1985. Numerical models on the influence of partial melt on elastic, anelastic and electric properties of rocks. Part I: elasticity and anelasticity. Phys. Earth Planet. Int. 41 (1), 34–57.

Shaw, P.R., Orcutt, J.A., 1985. Waveform inversion of seismic refraction data and applications to young Pacific crust. Geophys. J. R. Astr. Soc. 82, 375–414.

Smellie, J.L., 2001. Lithostratigraphy and volcanic evolution of Deception Island, South Shetland Islands. Antarct. Sci. 13 (2), 188–209.

Smellie, J.L., 2002a. Geology. In: Smellie, J.L., et al. (Ed.), Geology and Geomorphology of Deception Island. British Antarctic Survey, Cambridge, UK, pp. 11–30.

Smellie, J.L., 2002b. Volcanic hazard. In: Smellie, J.L., et al. (Ed.), Geology and Geomorphology of Deception Island. British Antarctic Survey, Cambridge, UK, pp. 47–53.

Smellie, J.L., Hofstetter, A., Troll, G., 1992. Fluorine and boron geochemistry of an ensialic marginal basin volcano: Deception Island, Bransfield Strait, Antarctica. J. Volcanol. Geotherm. Res. 49 (3–4), 255–267.

Smellie, J.L., et al., 2002. Geology and Geomorphology of Deception Island. BAS Geomap Series. British Antarctic Survey, Cambridge, UK. 78 pp.

Toomey, D.R., Solomon, S.C., Purdy, G.M., 1994. Tomographic imaging of the shallow crustal structure of the East Pacific Rise at 9°30′N. J. Geophys. Res. 99, 24,135–24,157.

Weiland, C.M., Steck, L.K., Dawson, P.B., Korneev, V.A., 1995. Nonlinear teleseismic tomography at Long Valley caldera, using three-dimensional minimum time travel time ray tracing. J. Geophys. Res. 100, 20,379–20,390.

West, M., Menke, W., Tolstoy, M., Webb, S., Sohn, R., 2001. Magma storage beneath Axial Volcano on the Juan de Fuca mid-ocean ridge. Nature 413, 833–836.

Wilcock, W.S.D., Solomon, S.C., Purdy, G.M., Toomey, D.R., 1995. Seismic attenuation structure of the East Pacific Rise near 9°30′N. J. Geophys. Res. 100, 24,147–24,165.

Zandomeneghi, D., et al., 2007. Three-dimensional P wave tomography of Deception Island Volcano, South Shetland Islands. In: Cooper, A.K., Raymond, C.R. (Eds.), Antarctica: A Keystone in a Changing World — Online Proceedings of the 10th ISAES, USGS Open-File Report 2007-1047, Extended Abstract 025. 5 pp.

Zandomeneghi, D. et al., submitted for publication. The Crustal Structure of Deception Island Volcano from P-wave Seismic Tomography: Tectonic and Volcanic Implications. J. Geophys. Res.